Quantum Simulation of an Extended Dicke Model with a Magnetic Solid

Nicolas Marquez Peraca,[1,*] Xinwei Li,[2,†] Jaime M. Moya,[1,3,*] Kenji Hayashida,[4,5,*] Xiaoxuan Ma,[6] Kelly J. Neubauer,[1] Diego Fallas Padilla,[1] Chien-Lung Huang,[1,7] Pengcheng Dai,[1] Andriy H. Nevidomskyy,[1] Han Pu,[1] Emilia Morosan,[1,3,8] Shixun Cao,[6,‡] Motoaki Bamba,[9,10,11,§] and Junichiro Kono[1,5,3,12,¶]

[1]*Department of Physics and Astronomy, Rice University, Houston, TX 77005, USA*
[2]*Department of Physics, California Institute of Technology, Pasadena, CA 91125, USA*
[3]*Smalley-Curl Institute, Rice University, Houston, TX 77005, USA*
[4]*Division of Applied Physics, Graduate School of Engineering, Hokkaido University, Hokkaido, 060-8628, Japan*
[5]*Department of Electrical and Computer Engineering, Rice University, Houston, TX 77005, USA*
[6]*Department of Physics, International Center of Quantum and Molecular Structures, and Materials Genome Institute, Shanghai University, Shanghai, 200444, China*
[7]*Department of Physics and Center for Quantum Frontiers of Research and Technology, National Cheng Kung University, Tainan 701, Taiwan*
[8]*Department of Chemistry, Rice University, Houston, TX 77005, USA*
[9]*Department of Physics I, Kyoto University, Kyoto 606-8502, Japan*
[10]*The Hakubi Center for Advanced Research, Kyoto University, Kyoto 606-8501, Japan*
[11]*PRESTO, Japan Science and Technology Agency, Saitama 332-0012, Japan*
[12]*Department of Materials Science and NanoEngineering, Rice University, Houston, TX 77005, USA*

(Dated: February 14, 2023)

The Dicke model describes the cooperative interaction of an ensemble of two-level atoms with a single-mode photonic field and exhibits a quantum phase transition as a function of light–matter coupling strength. Extending this model by incorporating short-range atom–atom interactions makes the problem intractable but is expected to produce new phases. Here, we simulate such an extended Dicke model using a crystal of $ErFeO_3$, where the role of atoms (photons) is played by Er^{3+} spins (Fe^{3+} magnons). Through magnetocaloric effect and terahertz magnetospectroscopy measurements, we demonstrated the existence of a novel atomically ordered phase in addition to the superradiant and normal phases that are expected from the standard Dicke model. Further, we elucidated the nature of the phase boundaries in the temperature–magnetic-field phase diagram, identifying both first-order and second-order phase transitions. These results lay the foundation for studying multiatomic quantum optics models using well-characterized many-body condensed matter systems.

The Dicke model in quantum optics describes the cooperative, coherent coupling of an ensemble of two-level atoms with a single-mode light field [1]. Despite its simplicity, the model hosts a rich variety of phenomena that are significant in diverse contexts, such as cavity quantum electrodynamics [2], condensed matter physics [3], and quantum information science [4, 5]. A prominent feature of the model is a second-order quantum phase transition (QPT), known as the superradiant phase transition (SRPT), which occurs when the light–matter coupling strength, g, exceeds a threshold [6, 7]. When the system enters the superradiant phase, atomic and photonic polarizations spontaneously emerge, producing a unique many-body ground state that enables studies of unusual light–matter entanglement [8], two-mode squeezed states [9–11], and quantum chaos [12].

Although the atomic ensemble in the original Dicke model was assumed to be noninteracting, it has been known from the early days that atom–atom interactions are important for explaining, for example, the dephasing and intensity correlation functions of fluorescent spectra [13, 14]. Hence, there has long been interest in extending the Dicke model to include an atom–atom interaction (represented by strength J); see Fig. 1. Such an extended Dicke model, or the g–J model, should display an interplay of two types of interatomic interactions – i.e., the photonic-field-mediated *long-range* interaction, and the direct *short-range* interaction. Intuitively, one can expect the ground state of the system to crucially depend on the ratio g/J, with a superradiant phase (an atomically ordered phase) favored for large (small) g/J. However, no analytical solutions can be obtained for the g–J model, motivating one to simulate it using a well-characterized many-body quantum system.

Computational studies of the g–J model under various approximations have revealed an array of new phenomena, such as a first-order QPT [15–19], a shift of the SRPT boundary [20, 21], amplification of the integrablity-to-chaos transition [22], modifications of matter–matter entanglement [20, 23], and alteration of the nature of an excited-state QPT [18, 24]. Mean-field solutions to the g–J model framed in complex networks have implications even for social sciences [25], describing opinion formation within the communicating agents of a social group sharing a common information field. To examine these phenomena, several experimental platforms, including atomic Bose–Einstein condensates [26, 27], superconducting qubits [28, 29], and quantum dots [15],

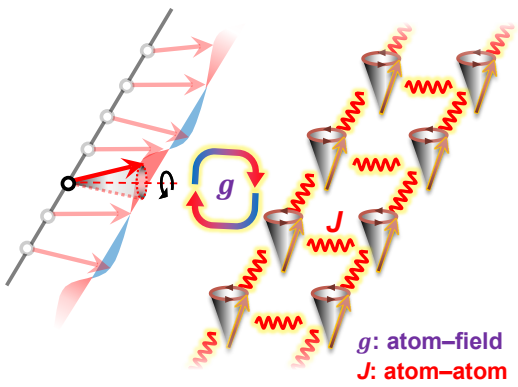

FIG. 1. The extended Dicke model, or the g–J model, where an ensemble of mutually interacting two-level atoms collectively couples with a bosonic field. The cooperative boson–atom interaction, with strength g, mediates long-range atom–atom interactions, whereas the direct atom–atom interaction, with strength J, is short-ranged.

have been proposed as quantum simulators, but successful simulations have not been achieved.

Here, we present a novel protocol of using a crystal of erbium orthoferrite ($ErFeO_3$), an antiferromagnetic (AFM) insulator, as a solid-state quantum simulator of the g–J model. The magnetic properties of $ErFeO_3$ are governed by the moments carried by the Er^{3+} and Fe^{3+} spin subsystems and their interplay [30]. A previous study has revealed Dicke cooperativity in the Er^{3+}–Fe^{3+} interaction [31], demonstrating the resemblance of the magnetic Hamiltonian of $ErFeO_3$ to the Dicke Hamiltonian. Namely, the paramagnetic Er^{3+} ions (the magnons of ordered Fe^{3+} spins) play the role of the atomic ensemble (light field), and the spin–magnon interaction is formally similar to the g-term in the Dicke model. What further strengthens this analogy is a magnetic phase transition of the crystal that exhibits all traits that would be expected for a Dicke SRPT. When the temperature (T) becomes lower than 4 K, the Er^{3+} lattice develops C-type AFM order [32] (with the ferromagnetic chains along z), and a zone-boundary Fe^{3+} magnon mode condenses, displacing the staggered moments away from the xz plane [33, 34]; this corresponds to the emergence of atomic and photon polarizations in the standard SRPT. In Bertaut's notation, the magnetic transition is of the $\Gamma_2 \rightarrow \Gamma_{12}$ type [Fig. 2(a)]. Mean-field calculations using a realistic spin model captures the simultaneous order parameter (OP) onsets of both the Er^{3+} and Fe^{3+} spin components, $\langle\Sigma_z^-\rangle$ and $\langle S_y\rangle$, respectively [Fig. 2(b)], indicating that the $\Gamma_2 \rightarrow \Gamma_{12}$ transition is a magnonic SRPT [35], with the Γ_2 and Γ_{12} phases corresponding to the normal (N) and superradiant (S) phases, respectively.

The J-term is inherently built into the magnetic Hamiltonian of $ErFeO_3$ since the Er^{3+}–Er^{3+} exchange interaction, albeit being weak, is known to be present [36]. Spectroscopic measurements have also revealed a fine frequency splitting within the Er^{3+} electron paramagnetic resonance lines [31], which is attributable to the Er^{3+}–Er^{3+} exchange interaction. The presence of both the g- and J-terms sets the stage for $ErFeO_3$ to simulate the g–J model. Nonetheless, although the g-term-driven S phase can find correspondence to the Γ_{12} phase in $ErFeO_3$, the g/J ratio set for the crystal stipulates that a pure atomic (A) phase, which is driven exclusively by the J-term, would not appear in equilibrium. For $ErFeO_3$, the A phase would be an Er^{3+} ordered phase *without involving any OP onset in the* Fe^{3+} *subsystem*. Therefore, to achieve quantum simulation of the g–J model, we must search for a way to invoke an explicit A phase through an S→A transition.

Our theoretical consideration suggests that subjecting $ErFeO_3$ to a static magnetic field (H) along the z axis can potentially induce an S→A transition. This can be understood by writing the simplified magnetic Hamiltonian [37] in the second-quantized form as

$$\hat{\mathcal{H}}/\hbar = \omega_\pi \hat{a}_\pi^\dagger \hat{a}_\pi + \omega_{\rm Er}\hat{\Sigma}_x^+ + \omega_z\hat{\Sigma}_z^+ + g\sqrt{\frac{2}{N_0}}i(\hat{a}_\pi^\dagger - \hat{a}_\pi)\hat{\Sigma}_z^- + J\frac{6}{N_0\hbar}[(\hat{\Sigma}_x^+)^2 + (\hat{\Sigma}_z^+)^2 - (\hat{\Sigma}_x^-)^2 - (\hat{\Sigma}_z^-)^2], \quad (1)$$

where a two-sublattice approximation is adopted for both Er^{3+} and Fe^{3+} for a total of N_0 unit cells. Here, ω_π, $\hat{a}_\pi^\dagger$, and $\hat{a}_\pi$ are the energy, creation and annihilation operators for the Fe^{3+} quasi-antiferromagnetic (qAFM) magnon mode, respectively; $\omega_{\rm Er}$ is the frequency of Er^{3+} spins as two-level systems at $H = 0$; $\omega_z = |\mathfrak{g}_z\mu_{\rm B}\mu_0 H|/\hbar$, where $\mathfrak{g}_z$ is the Landè g factor, $\mu_{\rm B}$ is the Bohr magneton, and μ_0 is the vacuum permeability, is the H-induced Zeeman frequency of Er^{3+}; and g and J are the Er^{3+}–magnon and Er^{3+}–Er^{3+} coupling strengths, leading to the g- and J-terms of the g–J Hamiltonian, respectively. $\hat{\Sigma}_p = \sum_{i=1}^{2N_0}\hat{\sigma}_{i,p}/2$, where $\hat{\sigma}_p$ are Pauli matrices and $p \in \{x, y, z\}$, is the collective Er^{3+} spin operator, with its superscript "+" ("−") denoting the sum (difference) of the two sublattices. The way these operators appear in Eq. (1) is crucial for interpreting the ground-state energetics. Specifically, the g-term features a product of the Fe^{3+} magnon field operator $i(\hat{a}_\pi^\dagger - \hat{a}_\pi)$ and the $\hat{\Sigma}_z^-$ component of Er^{3+} spins, thereby favoring antiparallel alignment of Er^{3+} sublattices and Fe^{3+} magnon condensation in the S phase [the onsets of $\langle\hat{\Sigma}_z^-\rangle$ and $\langle S_y\rangle$ in Fig. 2(b)], whereas the J-term couples Er^{3+} antiferromagnetically; larger $\langle\hat{\Sigma}_x^-\rangle$ and $\langle\hat{\Sigma}_z^-\rangle$, where $\langle ...\rangle$ denotes expectation values, are energetically more favorable.

It is important to note that supplying the Zeeman term $\hat{\mathcal{H}}_{\rm Zeeman}/\hbar = \omega_z\hat{\Sigma}_z^+$ provides quantum controllability. The term promotes $|\langle\hat{\Sigma}_z^+\rangle|$, the net moment of Er^{3+} sublattices, through Zeeman coupling to $H \parallel z$. Due to

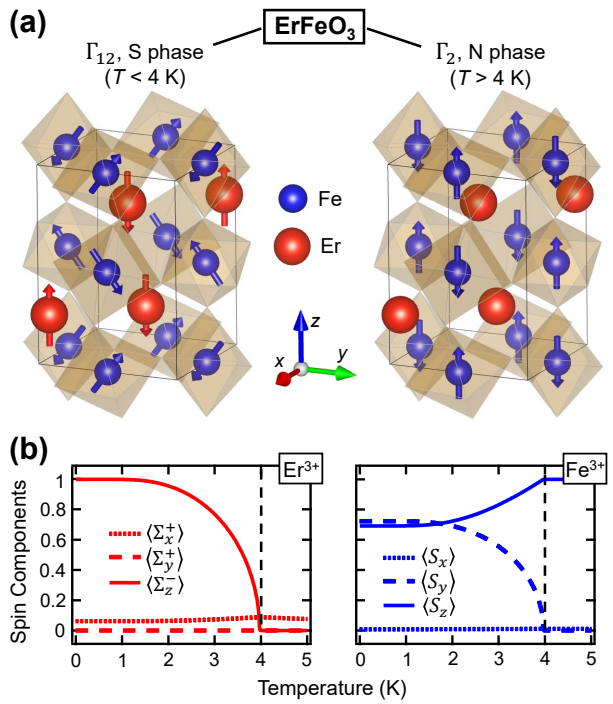

FIG. 2. $\Gamma_2 \to \Gamma_{12}$ transition in $ErFeO_3$ as a magnonic analog of the SRPT. (a) Lattice structure and spin configurations within the Γ_{12} and Γ_2 phases. Brown polyhedra represent octahedrally coordinated FeO_6 cages. (b) Temperature dependence of the Er^{3+} and Fe^{3+} spin components (normalized) across the phase transition at 0 T. $\hat{\Sigma}_p$, where $p \in \{x, y, z\}$, is the collective Er^{3+} spin operator, with its superscript "+" ("−") denoting the sum (difference) of the two sublattices. $\hat{S}_p$ are the components of Fe^{3+} spins.

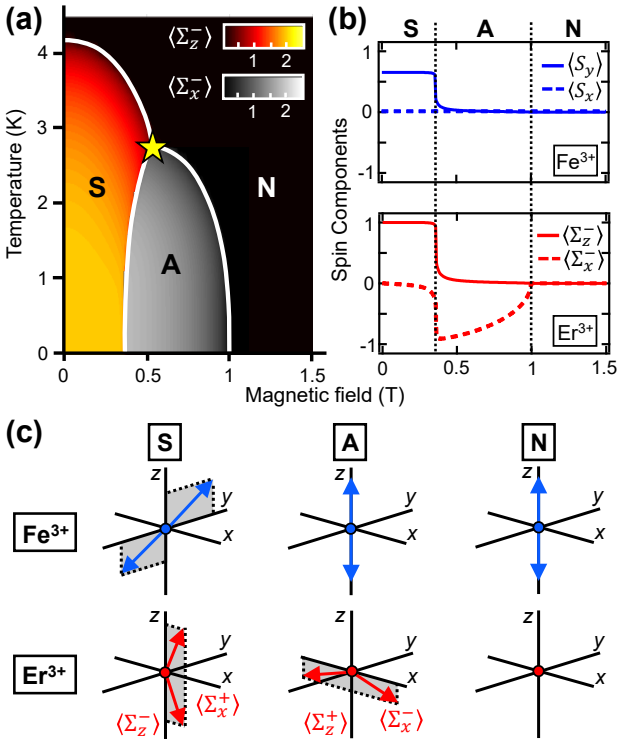

FIG. 3. Mean-field solution for the spin Hamiltonian of $ErFeO_3$ in $H \parallel z$. (a) Theoretical T-H phase diagram mapped by Er^{3+} spin components. (b) H-dependent evolution of the Er^{3+} and Fe^{3+} spin components (normalized) at $T = 0$ K. (c) Schematics of the spin configurations in each phase.

the commutation relation

$$[\hat{\Sigma}_z^+, \hat{\Sigma}_z^-] = 0 \neq [\hat{\Sigma}_z^+, \hat{\Sigma}_x^-], \tag{2}$$

modification to $\langle\hat{\Sigma}_z^+\rangle$ would impact $\langle\hat{\Sigma}_x^-\rangle$ much more than $\langle\hat{\Sigma}_z^-\rangle$. This would tip the balance between the g-term and the J-term, since $\hat{\Sigma}_x^-$ appears only in the J-term but not in the g-term.

As shown in Fig. 3(a), an S→A transition is indeed recovered in the calculated mean-field phase diagram of the spin Hamiltonian [37] within the T-$\mu_0 H$ parameter space, for $T < 2.8$ K, with a critical field ranging from 0.35 T to 0.5 T, depending on T. Increasing the field to above 1 T and elevating T to above 4 K would both push the system across the thermodynamic phase boundary into the N phase. A triple point (at 2.8 K and 0.5 T, decorated by a yellow star) marks the location where the S, A, and N phases converge. Figure 3(b) shows the calculated normalized spin components as the OPs of the magnetic phases, for a line cut along the H axis at $T = 0$ K, traversing sequentially the S→A and the A→N boundaries. We identify that the Fe^{3+} OP, represented by $\langle S_y\rangle$ (which is proportional to the magnon condensate density), is finite both in the S and A phases, but $\langle S_y\rangle \neq 0$ in the S phase and $\langle S_y\rangle \approx 0$ in the A phase. The Er^{3+} OP, on the other hand, is finite in both the S and A phases, but undergoes a switch from the $\langle\hat{\Sigma}_z^-\rangle \neq 0$, $\langle\hat{\Sigma}_x^-\rangle \approx 0$ type (S phase) to the $\langle\hat{\Sigma}_z^-\rangle \approx 0$, $\langle\hat{\Sigma}_x^-\rangle \neq 0$ type (A phase). Further, the OP evolution indicates that the S→A boundary is an abrupt-type, first-order phase transition, while the A→N boundary is a continuous-type, second-order phase transition.

Summarizing the mean-field calculation results, Fig. 3(c) pictorially shows the predicted Fe^{3+} and Er^{3+} spin order in each phase. Starting from the N phase, the two sublattices of Fe^{3+} are antiparallel along z with zero y-component, while Er^{3+} spins remain paramagnetic (no order). The A phase is characterized by Fe^{3+} order that is identical to that of the N phase, but the Er^{3+} subsystem develops canted AFM order where the sublattice moments are antiparallel along x ($\langle\hat{\Sigma}_x^-\rangle \neq 0$), with canting along z ($\langle\hat{\Sigma}_z^+\rangle \neq 0$). In the S phase, the Er^{3+} order takes the $\langle\hat{\Sigma}_x^+\rangle \neq 0$, $\langle\hat{\Sigma}_z^-\rangle \neq 0$ configuration, and the staggered moment of the Fe^{3+} sublattices undergoes a rotation about the x axis, bringing its y-component to nonzero, exactly corresponding to the formation of a qAFM magnon condensate.

We performed magnetocaloric effect (MCE) and ter-

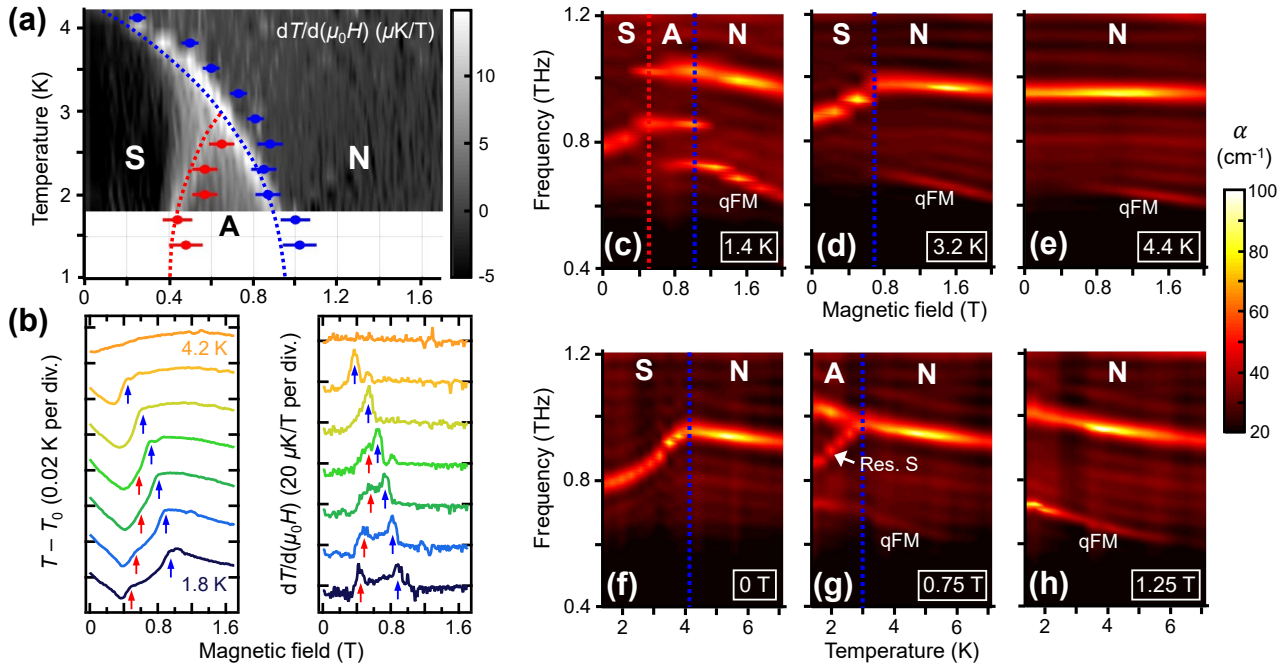

FIG. 4. (a) Experimental T-H phase diagram of $ErFeO_3$ in $H \parallel z$. Phase boundaries determined by THz measurements (solid circles) are overlaid on the $dT/d(\mu_0 H)$ color map determined from MCE measurements. Red (blue) dashed line denotes a first- (second-) order phase boundary. (b) MCE data traces at select temperatures (1.8 K to 4.2 K with 0.4 K interval) showing $T - T_0$ (T_0 being the initial temperature) vs $\mu_0 H$ (left) and $dT/d(\mu_0 H)$ vs $\mu_0 H$ (right); curves are offset. Red and blue arrows mark the boundaries outlined by red and blue dashed lines in (a), respectively. (c)-(e) THz absorption spectra mapped vs $\mu_0 H$ for select T values. (f)-(h) THz absorption spectra mapped vs T for select $\mu_0 H$ values. Red and blue dashed lines mark the same boundaries as those in (a). All features except for those labeled "qFM" are qAFM modes of Fe^{3+}.

ahertz (THz) magnetospectroscopy experiments to map out the T-H phase diagram of $ErFeO_3$, and the obtained results are summarized in Fig. 4(a). MCE measurements capture the differential change in sample temperature with respect to the magnetic field, $\mu_0^{-1}(\partial T/\partial H)_S$, which is a sensitive reporter of the magnetic entropy landscape. We configured a MCE measurement in a Physical Property Measurement System in the quasi-adiabatic condition, and took raw data traces of sample temperature variation versus magnetic field at a ramping rate of 5×10^{-3} T/s with $dH > 0$ [Fig. 4(b) left]; the sensitivity of temperature variation of our instrument reached 5×10^{-4} K. To identify H-induced phase transitions, the first-order derivative $dT/d(\mu_0 H)$ traces were computed [Fig. 4(b) right], whose local extremes correspond to the transition boundaries [38]. The traces clearly exhibit two maxima for $T < 2.8$ K, corresponding to the S→A [red arrows in Fig. 4(b) and red dashed line in Fig. 4(a)] and A→N (blue arrows and blue dashed line) boundaries, and one maximum for 2.8 K $< T <$ 4 K, corresponding to the S→N (blue arrows and blue dashed line) boundary.

THz magnetospectroscopy experiments provided additional details on the nature of the transition boundaries and the spin order in each phase. The measurements were performed on a z-cut $ErFeO_3$ crystal using a transmission-type THz time-domain spectrometer in the Faraday geometry. Absorption coefficient (α) spectra, derived from the imaginary part of the refractive index [37], were measured within the same T-H parameter space as that of the MCE experiments. Figures 4(c)-(e) and Figs. 4(f)-(h) show the H-dependence of α spectra at select T values and the T-dependence of α spectra at select $\mu_0 H$ values, respectively. We found that the bright absorption lines can be assigned to either the quasi-ferromagnetic (qFM) mode or the qAFM mode, which have been thoroughly studied in previous studies [39]. It is the evolution of these modes in distinct phases of the g–J model that is of interest here.

In the H-dependent color map at 1.4 K [Fig. 4(c)], three lines are observed. The lowest frequency line, which does not pick up intensity until 0.8 T, is the qFM mode, while the other two are both qAFM magnons, albeit belonging to distinct phases. The middle (upper) line, which is located at 0.8 THz at 0 T (1 THz at 0.5 T), is the qAFM mode of the S (A & N) phase. The S→A transition is identified to occur at 0.5 T (red dashed line) where the upper line emerges. The qAFM magnons belonging to the S and A phases coexist within 0.5 T $< \mu_0 H <$ 1 T,

consistent with the prediction that the S→A transition is of first order and is thus inhomogeneous, until the middle line vanishes at >1 T (blue dashed line) owing to entrance into the N phase. The 3.2 K map [Fig. 4(d)] shows a different behavior; the qAFM magnon (0.88 THz at 0 T) of the S phase continuously shifts to connect with that of the N phase in frequency, forming an OP-like onset for $\mu_0 H < 0.7$ T (blue dashed line), signaling a second-order N→S transition boundary. Such a frequency shift is absent in the 4.4 K map [Fig. 4(e)] since the N phase persists throughout the whole H range.

T-dependent color maps at constant H further corroborate our assignments of the phase transitions. Starting from the 0 T map [Fig. 4(f)], a continuous OP-like onset of the qAFM mode shift is again observed at the N→S transition boundary (< 4 K, blue dashed line). This echoes Fig. 4(d) in showing the continuous nature of the N→S transition, and establishes that the frequency shift of the qAFM magnon in the S phase from that in the N phase is a sensitive reporter of the qAFM magnon condensate density, namely, the Fe^{3+} OP of the S phase. Intriguingly, this OP is demonstrated to be zero in the A phase. We read this fact from the 0.75 T map [Fig. 4(g)], for which an N→A transition is expected upon lowering T. Although a residual mode pertaining to the S phase exists [as mentioned earlier when discussing Fig. 4(c)], the qAFM mode (unlabeled line) frequency does not undergo any noticeable OP-like anomaly across the N→A transition; it is as featureless as the qAFM mode within the 1.25 T map [Fig. 4(h)], for which the N phase persists throughout the whole T range. This unambiguously demonstrates that the spin order in the A phase only involves Er^{3+} ordering but not any Fe^{3+} OP, consistent with our expectation depicted in Fig. 3. Finally, phase boundaries determined by the THz experiments are overlaid (as solid circles) on top of the MCE phase diagram in Fig. 4(a), showing overall agreement.

In summary, through magnetocaloric effect and THz magnetospectroscopy experiments, we studied a crystal of $ErFeO_3$ to simulate the g–J model, which is an extended Dicke model that includes not only the bosonic-field-mediated long-range interatomic interactions but also direct short-range interactomic interactions. In addition to the superradiant and normal phases expected from the standard Dicke model, we identified a new phase, an atomic phase, which is driven by the short-range J-term in the Hamiltonian. Further, we elucidated the nature of the various phase boundaries, distinguishing between first-order and second-order transitions. These results demonstrated the potential of $ErFeO_3$ as a unique simulator of quantum optics Hamiltonians. More specifically, in the context of Dicke physics, this condensed matter platform may lead to the possibilities of assisting quantum chaos [22] and modifying matter–matter entanglement [20, 23] with tunability given by an external magnetic field. Bridging the gap between quantum optics and many-body correlated physics, our results will find broader application in the design of hybrid quantum systems with superior controllability, such as the Dicke-Ising machine [28, 40] and the Dicke-Lipkin-Meshkov-Glick model [18, 23]. Furthermore, the ability to transition between the superradiant and atomic phases via a nonthermal knob provides opportunities to study unconventional quantum criticality [41] and chaos-assisted thermalization [42].

We thank Shiming Lei, Andrey Baydin, Takuma Makihara, Dasom Kim, Fuyang Tay, and Timothy Noe for useful discussions. J.K. acknowledges support from the W. M. Keck Foundation (through Award No. 995764) and the Robert A. Welch Foundation (through Grant No. C-1509). X.L. acknowledges support from the Caltech Postdoctoral Prize Fellowship and the IQIM. S.C. is grateful for financial support from the National Natural Science Foundation of China (NSFC, No. 12074242), and the Science and Technology Commission of Shanghai Municipality (No. 21JC1402600). M.B. acknowledges support from the JST PRESTO program (Grant JPMJPR1767). J.M.M. was supported by the National Science Foundation Graduate Research Fellowship under Grant DGE 1842494. A.H.N. was supported by the Robert A. Welch Foundation (through Grant No. C-1818) and the US National Science Foundation (through Grant No. DMR-1917511). P.D. was supported by U.S. DOE BES DE-SC0012311.

* equal contributions
† equal contributions; email: xinweili@caltech.edu
‡ email: sxcao@shu.edu.cn
§ email: bamba.motoaki.y13@kyoto-u.jp
¶ email: kono@rice.edu

[1] R. H. Dicke, Phys. Rev. **93**, 99 (1954).
[2] B. M. Garraway, Philos. Trans. Royal Soc. A: Mathematical, Physical and Engineering Sciences **369**, 1137 (2011).
[3] K. Cong, Q. Zhang, Y. Wang, G. T. Noe, A. Belyanin, and J. Kono, J. Opt. Soc. Am. B **33**, C80 (2016).
[4] P. Forn-Díaz, L. Lamata, E. Rico, J. Kono, and E. Solano, Rev. Mod. Phys. **91**, 025005 (2019).
[5] A. Frisk Kockum, A. Miranowicz, S. De Liberato, S. Savasta, and F. Nori, Nat. Rev. Phys. **1**, 19 (2019).
[6] K. Hepp and E. H. Lieb, Ann. Phys. **76**, 360 (1973).
[7] Y. K. Wang and F. T. Hioe, Phys. Rev. A **7**, 831 (1973).
[8] N. Lambert, C. Emary, and T. Brandes, Phys. Rev. Lett. **92**, 073602 (2004).
[9] M. Artoni and J. L. Birman, Phys. Rev. B **44**, 3736 (1991).
[10] T. Makihara, K. Hayashida, G. T. Noe II, X. Li, N. Marquez Peraca, X. Ma, Z. Jin, W. Ren, G. Ma, I. Katayama, J. Takeda, H. Nojiri, D. Turchinovich, S. Cao, M. Bamba, and J. Kono, Nat. Commun. **12**, 3115 (2021).
[11] K. Hayashida, T. Makihara, N. M. Peraca, D. F. Padilla, H. Pu, J. Kono, and M. Bamba, Sci. Rep. **to appear** (2023).

[12] C. Emary and T. Brandes, Phys. Rev. Lett. **90**, 044101 (2003).
[13] R. Friedberg and S. R. Hartmann, Phys. Rev. A **10**, 1728 (1974).
[14] S. V. Lawande, B. N. Jagatap, and R. R. Puri, J. Phys. B: At. Mol. Phys. **18**, 1711 (1985).
[15] C. F. Lee and N. F. Johnson, Phys. Rev. Lett. **93**, 083001 (2004).
[16] Q.-H. Chen, T. Liu, Y.-Y. Zhang, and K.-L. Wang, Phys. Rev. A **82**, 053841 (2010).
[17] L.-P. Yang and Z. Jacob, Opt. Express **27**, 10482 (2019).
[18] R. Herrera Romero, M. A. Bastarrachea-Magnani, and R. Linares, Entropy **24**, 1198 (2022).
[19] X.-Q. Zhao, N. Liu, and J.-Q. Liang, Commun. Theor. Phys. **67**, 511 (2017).
[20] J. Nie, X. Huang, and X. Yi, Opt. Commun. **282**, 1478 (2009).
[21] G. Chen, D. Zhao, and Z. Chen, J. Phys. B: At., Mol. Opt. Phys. **39**, 3315 (2006).
[22] Q. Wang, Entropy **24**, 1415 (2022).
[23] R. A. Robles Robles, S. A. Chilingaryan, B. M. Rodríguez-Lara, and R.-K. Lee, Phys. Rev. A **91**, 033819 (2015).
[24] J. P. J. Rodriguez, S. A. Chilingaryan, and B. M. Rodríguez-Lara, Phys. Rev. A **98**, 043805 (2018).
[25] A. Y. Bazhenov, D. V. Tsarev, and A. P. Alodjants, Phys. Rev. E **103**, 062309 (2021).
[26] G. Chen, Z. Chen, and J.-Q. Liang, Europhys. Lett. **80**, 40004 (2007).
[27] B. M. Rodríguez-Lara and R.-K. Lee, Phys. Rev. E **84**, 016225 (2011).
[28] Y. Zhang, L. Yu, J. Q. Liang, G. Chen, S. Jia, and F. Nori, Sci. Rep. **4**, 4083 (2014).
[29] L. Tian, Phys. Rev. Lett. **105**, 167001 (2010).
[30] R. L. White, Journal of Applied Physics **40**, 1061 (1969).
[31] X. Li, M. Bamba, N. Yuan, Q. Zhang, Y. Zhao, M. Xiang, K. Xu, Z. Jin, W. Ren, G. Ma, S. Cao, D. Turchinovich, and J. Kono, Science **361**, 794 (2018).
[32] M. P. Zic, W. T. Fuhrman, K. Wang, S. Ran, J. Paglione, and N. P. Butch, J. Appl. Phys. **130**, 014102 (2021).
[33] G. Deng, P. Guo, W. Ren, S. Cao, H. E. Maynard-Casely, M. Avdeev, and G. J. McIntyre, Journal of Applied Physics **117**, 164105 (2015).
[34] V. Klochan, N. Kovtun, and V. Khmara, JETP **41**, 357 (1975).
[35] M. Bamba, X. Li, N. Marquez Peraca, and J. Kono, Commun. Phys. **5**, 3 (2022).
[36] A. M. Kadomtseva, I. B. Krynetskii, and V. M. Matveev, JETP **52**, 732 (1980).
[37] See Supplemental Material at [URL] for extensive simulation and experimental details.
[38] M. Jaime, K. H. Kim, G. Jorge, S. McCall, and J. A. Mydosh, Phys. Rev. Lett. **89**, 287201 (2002).
[39] X. Li, D. Kim, Y. Liu, and J. Kono, Photonics Insights **1**, R05 (2022).
[40] J. Rohn, M. Hörmann, C. Genes, and K. P. Schmidt, Phys. Rev. Res. **2**, 023131 (2020).
[41] Y. Xu and H. Pu, Phys. Rev. Lett. **122**, 193201 (2019).
[42] A. Altland and F. Haake, Phys. Rev. Lett. **108**, 073601 (2012).

Supplemental Material for "Quantum Simulation of an Extended Dicke Model with a Magnetic Solid"

Nicolas Marquez Peraca,[1] Xinwei Li,[2] Jaime M. Moya,[1,3] Kenji Hayashida,[4,5] Xiaoxuan Ma,[6] Kelly J. Neubauer,[1] Diego Fallas Padilla,[1] Chien-Lung Huang,[1,7] Pengcheng Dai,[1] Andriy H. Nevidomskyy,[1] Han Pu,[1] Emilia Morosan,[1,3,8] Shixun Cao,[6] Motoaki Bamba,[9,10,11] and Junichiro Kono[1,5,3,12]

[1]*Department of Physics and Astronomy, Rice University, Houston, TX 77005, USA*

[2]*Department of Physics, California Institute of Technology, Pasadena, CA 91125, USA*

[3]*Smalley-Curl Institute, Rice University, Houston, TX 77005, USA*

[4]*Division of Applied Physics, Graduate School of Engineering, Hokkaido University, Hokkaido, 060-8628, Japan*

[5]*Department of Electrical and Computer Engineering, Rice University, Houston, TX 77005, USA*

[6]*Department of Physics, International Center of Quantum and Molecular Structures, and Materials Genome Institute, Shanghai University, Shanghai, 200444, China*

[7]*Department of Physics and Center for Quantum Frontiers of Research and Technology, National Cheng Kung University, Tainan 701, Taiwan*

[8]*Department of Chemistry, Rice University, Houston, TX 77005, USA*

[9]*Department of Physics I, Kyoto University, Kyoto 606-8502, Japan*

[10]*The Hakubi Center for Advanced Research, Kyoto University, Kyoto 606-8501, Japan*

[11]*PRESTO, Japan Science and Technology Agency, Saitama 332-0012, Japan*

[12]*Department of Materials Science and NanoEngineering, Rice University, Houston, TX 77005, USA*

Contents

S1 Theoretical Model

In this section we briefly outline the steps of mapping the magnetic Hamiltonian of $ErFeO_3$ onto an extended Dicke model. Following prior work, the spin Hamiltonian taking into account all the spin subsystems and their mutual interactions is first introduced. The model is subsequently second quantized to have a form that resembles the extended Dicke Hamiltonian.

A. Spin Hamiltonian

We analyzed the $ErFeO_3$ spin system from a microscopic model originally derived in Ref. [1]. The total microscopic Hamiltonian is

$$\mathcal{H} = \mathcal{H}_{\mathrm{Fe}} + \mathcal{H}_{\mathrm{Er}} + \mathcal{H}_{\mathrm{Fe-Er}}. \tag{S1}$$

$\mathcal{H}_{\mathrm{Fe}}$, $\mathcal{H}_{\mathrm{Er}}$, and $\mathcal{H}_{\mathrm{Fe}}$ are Fe^{3+}, Er^{3+}, and Fe^{3+}–Er^{3+} interaction Hamiltonian, respectively. As in our previous studies [2, 3] and Herrmann's model [4], we take the two-sublattice model both for Er and Fe spins.

The Fe^{3+} Hamiltonian is

$$\begin{aligned}
\mathcal{H}_{\mathrm{Fe}} = & \sum_{s=\mathrm{A,B}} \sum_{i=1}^{N_0} \mu_{\mathrm{B}} \mu_0 \hat{\boldsymbol{S}}_i^s \cdot \mathfrak{g}^{\mathrm{Fe}} \boldsymbol{H} + J_{\mathrm{Fe}} \sum_{\mathrm{n.n.}} \hat{\boldsymbol{S}}_i^{\mathrm{A}} \cdot \hat{\boldsymbol{S}}_{i'}^{\mathrm{B}} \\
& - D_y^{\mathrm{Fe}} \sum_{\mathrm{n.n.}} \left(\hat{S}_{i,z}^{\mathrm{A}} \hat{S}_{i',x}^{\mathrm{B}} - \hat{S}_{i,z}^{\mathrm{B}} \hat{S}_{i',x}^{\mathrm{A}} \right) \\
& - \sum_{i=1}^{N_0} \left(A_x \hat{S}_{i,x}^{\mathrm{A}\,2} + A_z \hat{S}_{i,z}^{\mathrm{A}\,2} + A_{xz} \hat{S}_{i,x}^{\mathrm{A}} \quad \hat{S}_{i,z}^{\mathrm{A}} \quad \right) \\
& - \sum_{i=1}^{N_0} \left(A_x \hat{S}_{i,x}^{\mathrm{B}\,2} + A_z \hat{S}_{i,z}^{\mathrm{B}\,2} - A_{xz} \hat{S}_{i,x}^{\mathrm{B}} \quad \hat{S}_{i,z}^{\mathrm{B}} \quad \right).
\end{aligned}$$

$\hat{\boldsymbol{S}}_i^s$ is the Fe^{3+} spin operator with $S = 5/2$ at the i-th site and s sublattice. J_{Fe}, D_y^{Fe}, $A_{x(z,xz)}$ are a Fe^{3+} isotropic exchange constant, Dzyaloshinskii-Moriya interaction for the $y(b)$-axis, and the single ion anisotropy for the $x(z, xz)$ spin components. $\sum_{\mathrm{n.n.}}$ is a summation for the nearest neighbors and the number of nearest neighbors is $z_{\mathrm{Fe}} = 6$. N_0 is the number of

unit cells in $ErFeO_3$. The g-factor of Fe^{3+} is

$$\mathfrak{g}^{\mathrm{Fe}} = \begin{pmatrix} \mathfrak{g}_x^{\mathrm{Fe}} & 0 & 0 \\ 0 & \mathfrak{g}_y^{\mathrm{Fe}} & 0 \\ 0 & 0 & \mathfrak{g}_z^{\mathrm{Fe}} \end{pmatrix}.$$

μ_{B} is the Bohr magneton and $\boldsymbol{H}$ is an external magnetic field.

The Er^{3+} Hamiltonian is

$$\mathcal{H}_{\mathrm{Er}} = \sum_{s=\mathrm{A,B}} \sum_{i=1}^{N_0} \frac{\mu_0}{2} \hat{\boldsymbol{\sigma}}_i^{\mathrm{s}} \cdot \mathfrak{g}^{\mathrm{Er}} \cdot \boldsymbol{H} + J_{\mathrm{Er}} \sum_{\mathrm{n.n.}} \hat{\boldsymbol{\sigma}}_i^{\mathrm{A}} \cdot \hat{\boldsymbol{\sigma}}_{i'}^{\mathrm{B}}.$$

$\hat{\boldsymbol{\sigma}}_i^{\mathrm{s}}$ is the Er^{3+} spin operator at the i-th site and s sublattice. J_{Er} represents Er^{3+}–Er^{3+} isotorpic exchange constant. The g-factor of Er^{3+} is

$$\mathfrak{g}^{\mathrm{Er}} = \begin{pmatrix} \mathfrak{g}_x & 0 & 0 \\ 0 & \mathfrak{g}_y & 0 \\ 0 & 0 & \mathfrak{g}_z \end{pmatrix}.$$

Finally, the Fe^{3+}–Er^{3+} interaction Hamiltonian is

$$\mathcal{H}_{\mathrm{Er-Fe}} = \sum_{i=1}^{N_0} \sum_{s,s'=\mathrm{A,B}} \left[J \hat{\boldsymbol{\sigma}}_i^{\mathrm{s}} \cdot \hat{\boldsymbol{S}}^{s'} + \boldsymbol{D}^{s,s'} \cdot \left(\hat{\boldsymbol{\sigma}}_i^{\mathrm{s}} \times \hat{\boldsymbol{S}}^{s'} \right) \right].$$

In our Fe^{3+}–Er^{3+} interaction Hamiltonian, Fe^{3+} and Er^{3+} interact within the same unit cell. J is a Fe^{3+}–Er^{3+} isotropic exchange constant. $\boldsymbol{D}^{s,s'}$ is the Dzyaloshinskii-Moriya interaction and

$$\begin{aligned} \boldsymbol{D}^{\mathrm{A,A}} &= (D_x, D_y, 0)^t, \\ \boldsymbol{D}^{\mathrm{A,B}} &= (-D_x, -D_y, 0)^t, \\ \boldsymbol{D}^{\mathrm{B,A}} &= (-D_x, D_y, 0)^t, \\ \boldsymbol{D}^{\mathrm{B,B}} &= (D_x, -D_y, 0)^t. \end{aligned}$$

The state of spins are determined by the equations of motion in which we assume each individual spin experiences a uniform mean field supplied by its surrounding magnetic ions. Assuming the dynamics within all unit cells are identical, we can replace spins dependent on unit cells, $\boldsymbol{S}_i^s$ and $\boldsymbol{\sigma}_i^s$, with uniform spins, $\boldsymbol{S}^s$ and $\boldsymbol{\sigma}^s$ keeping the sublattice dependence.

From the Heisenberg equation from the Hamiltonian [Eq. (S1)], the equations of motion are

$$\hbar\frac{\partial}{\partial t}\boldsymbol{\sigma}^s = -\boldsymbol{\sigma}^s \times \mu_0 \mathfrak{g}\mu_B \boldsymbol{H}^s_{\mathrm{Er}}(\{\boldsymbol{\sigma}^{\mathrm{A/B}}\},\{\boldsymbol{S}^{\mathrm{A/B}}\}), \tag{S2}$$

$$\hbar\frac{\partial}{\partial t}\boldsymbol{S}^s = -\boldsymbol{S}^s \times \mu_0 \mathfrak{g}\mu_B \boldsymbol{H}^s_{\mathrm{Fe}}(\{\boldsymbol{\sigma}^{\mathrm{A/B}}\},\{\boldsymbol{S}^{\mathrm{A/B}}\}). \tag{S3}$$

$\mathfrak{g}$ is the free electron g-factor. $\boldsymbol{H}^s_{\mathrm{Er}}$ and $\boldsymbol{H}^s_{\mathrm{Fe}}$ are the mean-fields for Er^{3+} and Fe^{3+} spins, respectively. The mean-fields are defined as derivatives of the total Hamiltonian [Eq. (S1)] with respect to the corresponding spin variables, for example $g\mu_0\mu_{\mathrm{B}}\boldsymbol{H}^s_{\mathrm{Er}} = 2\partial\mathcal{H}/\partial\boldsymbol{\sigma}^s$. The phase diagrams shown in Fig. 2 and 3 of the main text are calculated by the following procedure.

From the equations of motion, the equilibrium spins ($\bar{\boldsymbol{\sigma}}^{\mathrm{A/B}}$ and $\bar{\boldsymbol{S}}^{\mathrm{A/B}}$) are parallel to the mean-fields $\bar{\boldsymbol{H}}^s_{\mathrm{Er}} = \boldsymbol{H}^s_{\mathrm{Er}}(\{\bar{\boldsymbol{\sigma}}^{\mathrm{A/B}}\},\{\bar{\boldsymbol{S}}^{\mathrm{A/B}}\})$ and $\bar{\boldsymbol{H}}^s_{\mathrm{Fe}} = \boldsymbol{H}^s_{\mathrm{Fe}}(\{\bar{\boldsymbol{\sigma}}^{\mathrm{A/B}}\},\{\bar{\boldsymbol{S}}^{\mathrm{A/B}}\})$. They are connected as

$$\bar{\boldsymbol{\sigma}}^s = \langle\hat{\boldsymbol{\sigma}}^s\rangle = \langle\hat{\sigma}^s_{\parallel}\rangle\,\boldsymbol{u}^s_{\mathrm{Er}}, \quad \hat{\sigma}^s_{\parallel} = \hat{\boldsymbol{\sigma}}^s\cdot\boldsymbol{u}^s_{\mathrm{Er}}, \quad \boldsymbol{u}^s_{\mathrm{Er}} = \bar{\boldsymbol{H}}^s_{\mathrm{Er}}/|\bar{\boldsymbol{H}}^s_{\mathrm{Er}}|, \tag{S4}$$

$$\bar{\boldsymbol{S}}^s = \langle\hat{\boldsymbol{S}}^s\rangle = \langle\hat{S}^s_{\parallel}\rangle\,\boldsymbol{u}^s_{\mathrm{Fe}}, \quad \hat{S}^s_{\parallel} = \hat{\boldsymbol{S}}^s\cdot\boldsymbol{u}^s_{\mathrm{Fe}}, \quad \boldsymbol{u}^s_{\mathrm{Fe}} = \bar{\boldsymbol{H}}^s_{\mathrm{Fe}}/|\bar{\boldsymbol{H}}^s_{\mathrm{Fe}}|. \tag{S5}$$

We determine the equilibrium spins ($\bar{\boldsymbol{\sigma}}^{\mathrm{A/B}}$ and $\bar{\boldsymbol{S}}^{\mathrm{A/B}}$) in the following self-consistent equations

$$\langle\hat{\sigma}^s_{\parallel}\rangle = -\frac{\partial}{\partial y_s}\ln Z^s_{\mathrm{Er}} = -\tanh(y_s), \tag{S6}$$

$$\langle\hat{S}^s_{\parallel}\rangle = -\frac{\partial}{\partial x_s}\ln Z^s_{\mathrm{Fe}} = -SB_S(Sx_s), \tag{S7}$$

$B_J(z)$ is the Brillouin function

$$B_J(z) = \frac{2J+1}{2J}\coth\left(\frac{2J+1}{2J}z\right) - \frac{1}{2J}\coth\left(\frac{z}{2J}\right),$$

and the partition functions are

$$Z^s_{\mathrm{Er}} \equiv \mathrm{Tr}\left[\mathrm{e}^{-\hat{\mathcal{H}}^s_{\mathrm{Er}}/k_BT}\right] = \sum_{m=\pm1}\mathrm{e}^{-my_s} = 2\cosh(y_s), \tag{S8}$$

$$Z^s_{\mathrm{Fe}} \equiv \mathrm{Tr}\left[\mathrm{e}^{-\hat{\mathcal{H}}^s_{\mathrm{Fe}}/k_BT}\right] = \sum_{m=-S}^{S}\mathrm{e}^{-mx_s} = \frac{\sinh[(S+1/2)x_s]}{\sinh(x_s/2)}, \tag{S9}$$

$$y_s = \frac{\mathfrak{g}\mu_0\mu_B|\bar{\boldsymbol{H}}^s_{\mathrm{Er}}|}{2k_BT}, \quad x_s = \frac{\mathfrak{g}\mu_0\mu_B|\bar{\boldsymbol{H}}^s_{\mathrm{Fe}}|}{k_BT}.$$

k_B is Boltzmann constant and T is temperature. Finally, the effective Hamiltonians of given mean-fields $\bar{\boldsymbol{H}}^s_{\mathrm{Er}}$ and $\bar{\boldsymbol{H}}^s_{\mathrm{Fe}}$ are

$$\hat{\mathcal{H}}^s_{\mathrm{Er}} = \frac{1}{2}\mathfrak{g}\mu_0\mu_B\hat{\boldsymbol{\sigma}}^s \cdot \bar{\boldsymbol{H}}^s_{\mathrm{Er}} = \frac{1}{2}\mathfrak{g}\mu_0\mu_B\hat{\sigma}^s_{\parallel}|\bar{\boldsymbol{H}}^s_{\mathrm{Er}}|,$$
$$\hat{\mathcal{H}}^s_{\mathrm{Fe}} = \mathfrak{g}\mu_0\mu_B\hat{\boldsymbol{S}}^s \cdot \bar{\boldsymbol{H}}^s_{\mathrm{Fe}} = \mathfrak{g}\mu_0\mu_B\hat{S}^s_{\parallel}|\bar{\boldsymbol{H}}^s_{\mathrm{Fe}}|.$$

Here, $\hat{\boldsymbol{\sigma}}^s$ and $\hat{\boldsymbol{S}}^s$ are vectors of the Pauli operators and angular momentum with the magnitude S.

To determine the ground state, we calculate free energy from the partition functions, Eqs. (S8-S9), and pick the configuration with the lowest energy. The free energies are defined as

$$F^s_{\mathrm{Er}} = -k_BT\ln Z^s_{\mathrm{Er}},$$
$$F^s_{\mathrm{Fe}} = -k_BT\ln Z^s_{\mathrm{Fe}}.$$

The total free energy of Er^{3+} and Fe^{3+} spins are

$$F = \sum_{s=\mathrm{A,B}} \left(F^s_{\mathrm{Er}} + F^s_{\mathrm{Fe}}\right)/2. \tag{S10}$$

B. Extended Dicke model

Second quantization of the spin Hamiltonian Eq. S1 has been carried out by Ref. [1]. We omit the derivation here since details can be found in the reference. For the sake of consistency, notation will follow those in Ref. [1], but will be substituted by those used in Eq. 1 of the main text eventually. Ref. [1] expressed the total Hamiltonian as

$$\begin{aligned}\hat{\mathcal{H}} \approx &\sum_{K=0,\pi} \hbar\omega_K \hat{a}^\dagger_K\hat{a}_K + \omega_{\mathrm{Er}}\hat{\Sigma}^+_x + \sum_{\xi=x,y,z}\mathfrak{g}^{\mathrm{Er}}_\xi\mu_{\mathrm{B}}B^{\mathrm{DC}}_\xi\hat{\Sigma}^+_\xi \\ &+ \frac{8z_{\mathrm{Er}}J_{\mathrm{Er}}}{N}\hat{\boldsymbol{\Sigma}}^{\mathrm{A}}\cdot\hat{\boldsymbol{\Sigma}}^{\mathrm{B}} + \frac{2\hbar g_x}{\sqrt{N}}(\hat{a}^\dagger_\pi + \hat{a}_\pi)\hat{\Sigma}^+_x \\ &+ \frac{\mathrm{i}2\hbar g_y}{\sqrt{N}}(\hat{a}^\dagger_0 - \hat{a}_0)\hat{\Sigma}^+_y + \frac{2\hbar g'_y}{\sqrt{N}}(\hat{a}^\dagger_\pi + \hat{a}_\pi)\hat{\Sigma}^-_y \\ &+ \frac{\mathrm{i}2\hbar g_z}{\sqrt{N}}(\hat{a}^\dagger_\pi - \hat{a}_\pi)\hat{\Sigma}^-_z + \frac{2\hbar g'_z}{\sqrt{N}}(\hat{a}^\dagger_0 + \hat{a}_0)\hat{\Sigma}^+_z.\end{aligned} \tag{S11}$$

Here, $K = 0$ and π corresponds to the qFM and qAFM magnon modes. $\hat{\boldsymbol{\Sigma}}^{\mathrm{A/B}}$ is a spin-$\frac{N}{4}$ operator representing the rare-earth spins in the A/B sublattice, satisfying

$$\hat{\boldsymbol{\Sigma}}^{\mathrm{A/B}} \equiv \frac{1}{2}\sum_{i=1}^{N_0}\hat{\boldsymbol{R}}^{\mathrm{A/B}}_i, \tag{S12}$$

where $(1/2)\hat{\boldsymbol{R}}_i^{\mathrm{A/B}}$ is a spin-$\frac{1}{2}$ operator for an Er^{3+} ion. We also define the sum and difference of the two sublattice spins as

$$\hat{\boldsymbol{\Sigma}}^{\pm} \equiv \hat{\boldsymbol{\Sigma}}^{\mathrm{A}} \pm \hat{\boldsymbol{\Sigma}}^{\mathrm{B}}. \tag{S13}$$

The total number of spin-$\frac{1}{2}$ spins (Er^{3+} spins) in the two sublattices is

$$N \equiv 2N_0. \tag{S14}$$

The five Er^{3+}–magnon coupling terms were rewritten in terms of the annihilation (creation) operators $\hat{a}_K$ ($\hat{a}_K^\dagger$) of a magnon, with their respective coupling strengths defined as

$$\begin{aligned}
\hbar g_x &= \sqrt{2S}(J\cos\beta_0 - D_y \sin\beta_0)\left(\frac{b+a}{d-c}\right)^{1/4} \\
&= h \times 0.051 \text{ THz}, && \text{(S15a)} \\
\hbar g_y &= \sqrt{2S}J\left(\frac{d+c}{b-a}\right)^{1/4} \\
&= h \times 0.041 \text{ THz}, && \text{(S15b)} \\
\hbar g'_y &= \sqrt{2S}(D_x \sin\beta_0)\left(\frac{b+a}{d-c}\right)^{1/4} \\
&= h \times 3.1 \times 10^{-5} \text{ THz}, && \text{(S15c)} \\
\hbar g_z &= \sqrt{2S}D_x\left(\frac{d-c}{b+a}\right)^{1/4} \\
&= h \times 0.116 \text{ THz}, && \text{(S15d)} \\
\hbar g'_z &= \sqrt{2S}(-J\sin\beta_0 - D_y\cos\beta_0)\left(\frac{b-a}{d+c}\right)^{1/4} \\
&= h \times (-0.040 \text{ THz}). && \text{(S15e)}
\end{aligned}$$

The numerical values of these coupling strengths are evaluated by the set of parameters, a, b, c, d, J, β_0, D_x, D_y, which are defined and quantitatively given in Ref. [1]. We found that the $\hbar g_z$ is the dominant term, for which we retain in Eq. (1) in the main text and all other Fe^{3+}–Er^{3+} coupling terms are dropped as an approximation.

Regarding the Er^{3+}–Er^{3+} interaction term, while the Er^{3+} spin ensemble is described by six operators, $\hat{\Sigma}^+_{x,y,z}$ and $\hat{\Sigma}^-_{x,y,z}$, in the extended Dicke Hamiltonian, only $\hat{\Sigma}^+_x$ and $\hat{\Sigma}^-_z$ are relevant to the low temperature phase transition. $\hat{\Sigma}^+_x$ corresponds to the paramagnetic alignment by the Fe^{3+} magnetization along the a axis, and $\hat{\Sigma}^-_z$ corresponds to the antiferromagnetic ordering along the c axis. Then, for analyzing the thermal-equilibrium values of the

spins, we need to consider only the following terms in the Er^{3+}–Er^{3+} exchange interactions:

$$\frac{8z_{\rm Er}J_{\rm Er}}{N}\hat{\boldsymbol{\Sigma}}^{\rm A}\cdot\hat{\boldsymbol{\Sigma}}^{\rm B}=\frac{2z_{\rm Er}J_{\rm Er}}{N}\sum_{\xi=x,y,z}\left[(\hat{\Sigma}_{\xi}^{+})^2-(\hat{\Sigma}_{\xi}^{-})^2\right]$$
$$\rightarrow\frac{2z_{\rm Er}J_{\rm Er}}{N}\left[(\hat{\Sigma}_{x}^{+})^2+(\hat{\Sigma}_{z}^{+})^2-(\hat{\Sigma}_{x}^{-})^2-(\hat{\Sigma}_{z}^{-})^2\right]. \tag{S16}$$

After this substitution, a notation substitution of $g_z \rightarrow g$ and $J_{\rm Er} \rightarrow J$, and incorporating the aforementioned simplification about the coupling terms, Eq. S11 becomes Eq. (1) in the main text. Numerical values of the material parameters therein are:

$$J = 0.037 \text{ meV} \tag{S17}$$

$$g = 0.48 \text{ meV} \tag{S18}$$

$$\omega_{\pi} = 2\pi \times 0.896 \text{ THz} \tag{S19}$$

$$\omega_{\rm Er} = 2\pi \times 0.023 \text{ THz}. \tag{S20}$$

S2 Materials and Methods

A. Sample preparation

Polycrystalline $ErFeO_3$ was first synthesized by a conventional solid state reaction method using Er_2O_3 (99.9%) and Fe_2O_3 (99.98%) powders. According to the stoichiometric ratio, the original reagents were weighted carefully and pulverized with moderate anhydrous ethanol in an agate mortar. Mixtures were sintered at 1300 °C for 1000 minutes and then cooled down to room temperature. The sintered powders were thoroughly reground and pressed into a rod that is 70 mm in length and 5-6 mm in diameter by a Hydrostatic Press System (Riken Seiki CO. Ltd, model HP-M-SD-200) at 70 MPa, and then sintered again at 1300 °C for sufficient reaction. Single crystal sample was then grown by an optical floating zone furnace (FZT-10000-H-VI-P-SH, Crystal Systems Corp; heat source: four 1 kW halogen lamps). The polycrystalline samples were melted in an airflow. Conditions like the melting power and the rate of sample rotation were stabilized and controlled in the molten zone.

B. THz Magnetospectroscopy

We performed time-domain THz transmission magnetospectroscopy measurements in the Faraday geometry. The sample is placed in a liquid-helium-cooled magneto-optical cryostat

(Oxford Instruments Spectromag-10T) with variable temperatures T between 1.4 and 300 K and static magnetic fields $\mu_0 H$ up to 10 T. We generate THz pulses via optical rectification using a Ti:sapphire regenerative amplifier (775 nm, 0.7 mJ, 150 fs, 1 kHz, Clark-MXR, Inc., CPA2001) as a laser source that pumps a (110) zinc telluride (ZnTe) crystal, while detection is accomplished through electro-optical sampling in another ZnTe crystal.

Index of Refraction and Absorption Coefficient

In this section we derive the standard equations used in the extraction of the complex index of refraction of a sample using THz-TDS. Let $\tilde{E}_0(\omega)$ be the Fourier transform of an incoming THz pulse $E_0(t)$ incident on two linear media surrounding a homogeneous dielectric slab of thickness d (the sample). We assume that trailing pulses due to multiple reflections within the sample (the Fabry-Pérot effect) are well separated in time from the main transmitted THz pulse and that the incidence is normal to the sample surfaces (assumed parallel and flat). Experimentally, two separate measurements are consecutively carried out. First, the THz electric field transmitting without a sample in place is measured and the reference electric field $\tilde{E}_{\mathrm{r}}(\omega)$ is obtained. Second, both the sample and its surroundings is measured and $\tilde{E}_{\mathrm{s}}(\omega)$ is extracted. Under these assumptions, each transmitted electric field can be written as [5, 6]:

$$\tilde{E}_{\mathrm{r}}(\omega) = \tilde{t}_{13}(\omega)\tilde{P}_{\mathrm{vac}}(\omega, d)\tilde{E}_0(\omega) \tag{S21}$$

$$\tilde{E}_{\mathrm{s}}(\omega) = \tilde{t}_{12}(\omega)\tilde{P}_{\mathrm{s}}(\omega, d)\tilde{t}_{23}\tilde{E}_0(\omega) \tag{S22}$$

where $\tilde{t}_{jk} = \frac{2\tilde{n}_j}{\tilde{n}_j + \tilde{n}_k}$ is the complex Fresnel transmission coefficient between mediums j and k, $\tilde{P}_j(\omega, d_j) = e^{ik_0 d_j \tilde{n}_j} = e^{i(\omega d_j/c)\tilde{n}_j}$ is the propagator through medium j, and the subscripts vac, r, and s refer to vacuum, reference, and sample, respectively. The ratio between $\tilde{E}_{\mathrm{r}}(\omega)$ and $\tilde{E}_{\mathrm{s}}(\omega)$ is the transfer function $\tilde{H}(\omega)$, and it follows from Eqs. S21 and S22 that:

$$\tilde{H}(\omega) = \frac{\tilde{E}_{\mathrm{s}}(\omega)}{\tilde{E}_{\mathrm{r}}(\omega)} = \frac{\tilde{t}_{12}\tilde{t}_{23}}{\tilde{t}_{13}} \frac{\tilde{P}_{\mathrm{s}}(\omega, d)}{\tilde{P}_{\mathrm{vac}}(\omega, d)} = \frac{2\tilde{n}_2(\tilde{n}_1 + \tilde{n}_3)}{(\tilde{n}_1 + \tilde{n}_2)(\tilde{n}_2 + \tilde{n}_3)} e^{i(\omega d/c)(\tilde{n}_{\mathrm{s}} - 1)} \tag{S23}$$

The bulk samples characterized in this work are single crystals grown without a substrate, and therefore, the surrounding mediums can be taken as vacuum by setting $\tilde{n}_1 = \tilde{n}_3 = 1$ in Eq. S23. With this simplification, the coefficient in front of the exponential becomes $\frac{4\tilde{n}_{\mathrm{s}}}{(\tilde{n}_{\mathrm{s}}+1)^2}$, where we have change the subscript $\tilde{n}_2$ to $\tilde{n}_{\mathrm{s}}$ for convenience. Furthermore, we

can set $\tilde{n}_\mathrm{s} = n_\mathrm{s}(\omega)$ for $\tilde{t}_{jk}$ and solve Eq. S23 for $\tilde{n}_\mathrm{s} = n_\mathrm{s}(\omega) + i\kappa_\mathrm{s}(\omega)$ in the exponential. Here, $n_\mathrm{s}(\omega)$ is the index of refraction of the sample, and $\kappa_\mathrm{s}(\omega)$ its extinction coefficient. This approximation is justified by the fact that the sample absorption is negligible in the Fresnel transmission coefficient compared to the exponential term and is thus used in the data analysis here described. We obtain:

$$\tilde{H}(\omega) = \frac{4n_\mathrm{s}(\omega)}{(n_\mathrm{s}(\omega)+1)^2} e^{i(\omega d/c)(\tilde{n}_\mathrm{s}-1)} = \frac{4n_\mathrm{s}(\omega)}{(n_\mathrm{s}(\omega)+1)^2} e^{i(\omega d/c)(n_\mathrm{s}(\omega)-1)} e^{-(\omega d/c)\kappa_\mathrm{s}(\omega)} \tag{S24}$$

Taking the modulus and phase of Eq. S24 leads to:

$$\Phi[\tilde{H}(\omega)] = \left(\frac{\omega d}{c}\right)(n_\mathrm{s}(\omega)-1) \rightarrow n_\mathrm{s}(\omega) = 1 + \frac{c}{\omega d}\Phi[\tilde{H}(\omega)] \tag{S25}$$

$$|\tilde{H}(\omega)| = \frac{4n_\mathrm{s}(\omega)}{(n_\mathrm{s}(\omega)+1)^2} e^{-(\omega d/c)\kappa_\mathrm{s}(\omega)} \rightarrow \kappa_\mathrm{s}(\omega) = -\frac{c}{\omega d}\ln\left[\frac{(n_\mathrm{s}(\omega)+1)^2}{4n_\mathrm{s}(\omega)}|\tilde{H}(\omega)|\right] \tag{S26}$$

We can also re-write this result in terms of the absorption coefficient $\alpha(\omega)$ of the sample as:

$$n(\omega) = 1 + \frac{c}{\omega d}\Phi[\tilde{H}(\omega)] \tag{S27}$$

$$\alpha(\omega) = \frac{2\omega}{c}\kappa(\omega) = -\frac{2}{d}\ln\left[\frac{(n(\omega)+1)^2}{4n(\omega)}|\tilde{H}(\omega)|\right] \tag{S28}$$

where we have dropped the subscript s for convenience. In conclusion, by Fourier transforming $\tilde{E}_\mathrm{r}(t)$ and $\tilde{E}_\mathrm{s}(t)$, which are obtained experimentally, the transfer function $\tilde{H}(\omega)$ can be calculated as $\tilde{E}_\mathrm{s}(\omega)/\tilde{E}_\mathrm{r}(\omega)$, and $n(\omega)$ and $\alpha(\omega)$ follow from Eqs. S27 and S28, respectively.

[1] M. Bamba, X. Li, N. Marquez Peraca, and J. Kono, Commun. Phys. **5**, 3 (2022).

[2] X. Li, M. Bamba, N. Yuan, Q. Zhang, Y. Zhao, M. Xiang, K. Xu, Z. Jin, W. Ren, G. Ma, S. Cao, D. Turchinovich, and J. Kono, Science **361**, 794 (2018).

[3] M. Bamba, X. Li, and J. Kono, in *Ultrafast Phenomena and Nanophotonics XXIII*, Vol. 10916, edited by M. Betz and A. Y. Elezzabi, International Society for Optics and Photonics (SPIE, 2019) p. 1091605.

[4] G. Herrmann, Journal of Physics and Chemistry of Solids **24**, 597 (1963).

[5] M. Naftaly, *Terahertz Metrology*, Microwave engineering (Artech House, 2015).

[6] L. Duvillaret, F. Garet, and J.-L. Coutaz, IEEE Journal of Selected Topics in Quantum Electronics **2**, 739 (1996).